Appl. Phys. A 65, 477–485 (1997)

Applied Physics A Materials Science & Processing



# Mechanisms of absorption in pulsed excimer laser-induced plasma

**K.H. Song, X. Xu***

School of Mechanical Engineering, Purdue University, West Lafayette, IN 47907, USA
(Fax: +1-765/494 05 39, E-mail: xxu@ecn.purdue.edu)

Received: 20 January 1997/Accepted: 23 June 1997

**Abstract.** This work investigates the interaction between pulsed excimer laser-induced plasma and an excimer laser beam. The optical transmissivity through the laser-induced plasma and the velocity of the plasma front are measured within the duration of the laser pulse. Based on the measured velocity of the plasma front, an analysis of compressible gas dynamics is used to compute the thermodynamic properties of the plasma layer, including temperature, pressure, and the number density of the laser-evaporated particles. The absorption coefficient of each absorption mode in the plasma is then calculated from the thermodynamic properties. By comparing the calculated and the measured transmissivity of the laser-induced plasma, we have determined the dominant absorption mechanism in the plasma plume to be photo-ionization at laser intensities in the range 90–400 MW/cm$^2$.

**PACS:** 52.40.Nk; 52.50.Jm; 79.20.Ds

High-power excimer lasers are being used in a variety of applications, including pulsed laser deposition of thin films and laser-assisted machining. During these processes, the laser beam evaporates and ionizes the target material, creating a plasma plume above the target surface. Understanding the transport process of the laser beam in the laser-induced plasma plume is essential for controlling the interaction of the laser and the materials being used, and for optimizing the high-power laser processes. The objective of this work is to determine experimentally the optical absorption coefficient of the laser-induced plasma. Further, attempts are made to understand the absorption mechanism in the laser-induced plasma.

There are several reports on the optical properties of the laser-induced plume [1–3]. Most of the reported work has studied the optical properties of the laser-induced plasma in the period of time after the laser pulse is terminated. At several microseconds after the laser pulse, the physical dimension of the plume is large enough so that a probing light-source can pass through the plasma plume and detect its properties. On the other hand, understanding the laser–plasma interaction requires measurements of the optical properties of the plume within the duration of the laser pulse. The small dimension of the plasma layer before the termination of the laser pulse (less than a few hundred microns) is a major obstacle for performing diagnostic measurements. In this work, an experimental technique is developed to measure the transient optical properties of the laser-induced plasma before the termination of the laser pulse.

In order to analyze the absorption mechanisms of the laser-induced plasma, its thermodynamic properties, including temperature, pressure, and the number density of the laser-evaporated particles need to be known. Theoretical absorption coefficients of each absorption mode (photo- ionization, inverse bremsstrahlung, etc.) can be calculated from the thermodynamic properties, and can therefore be compared with the measured values in order to reveal the absorption mechanisms in the plasma. However, the thermodynamic properties of the laser-induced plasma are not readily measurable within the laser pulse. These properties are normally inferred from experimental data obtained after the laser pulse. In this work, the velocity of the laser-induced plasma is measured during the laser pulse. The thermodynamic properties are then calculated from the measured plasma velocity using a one-dimensional compressible gas dynamics analysis. This approach is different from many reported analytical studies of the laser-evaporation process [4–6], in which the gas dynamic equations are solved together with the energy equations in the target by using the laser intensity as the input parameter. The advantage of using the measured plasma velocity as the input parameter is that it does not require thermophysical properties and target surface conditions (temperature-dependent absorption coefficient, surface morphology, etc.), which are normally difficult to obtain. It is also shown in this work that the "abnormal" characteristics of the laser-evaporated plume are not readily predictable by the combined thermal and gas dynamics analysis.

The transient velocity of the laser-induced plasma is measured using the optical deflection technique. This method is chosen because other techniques, including high-speed photography, streak photography and the shadow graphic

*To whom all correspondence should be addressed

method, are only capable of capturing the image of a plume with large physical dimension. On the other hand, the optical deflection technique has a spatial resolution of the order of the width of a focused probing laser beam, which is about 10 μm in this work. The optical deflection technique senses the refractive index discontinuity caused by the laser-induced shock-wave and vapor, and thus it measures the transient locations as well as the velocity of the shock front and the vapor front.

The absorption coefficients of each absorption mode are estimated using the thermodynamic properties obtained from the gas dynamics analysis. Comparison between the measured and the calculated transmissivity allows determination of the absorption mechanisms in the laser-induced plasma. The laser intensity used in this work is limited in the range between 90 MW/cm$^2$ and 400 MW/cm$^2$ (2–11 J/cm$^2$ for a laser pulse with FWHM of 26 ns). Nickel is used as the specimen.

## 1 Experimental descriptions

Figure 1 shows the experimental setup for measuring the velocity of the laser-induced plasma. The KrF excimer laser has a wavelength at 248 nm and a pulse width of 26 ns (FWHM). The center, uniform portion of the excimer laser beam passes through a rectangular aperture (10 mm × 5 mm) to produce a laser beam with a uniform intensity profile. The rectangular laser beam is focused onto the nickel specimen and evaporates the target surface. (The laser-evaporated surface was examined under an optical microscope, and the central 90% of the laser-irradiated area was found to be uniform.) The laser intensity is changed by varying the distance between the lens and the target surface. The probing laser for the optical deflection measurement is a 5 mW, He−Ne laser with a wavelength at 633 nm. The He−Ne laser beam is focused to a 10 μm spot above the nickel target surface, and its intensity is measured by a photodiode. A narrow-band filter at the He−Ne laser wavelength is positioned in front of the detecting photodiode to eliminate the plasma emission. The laser-induced shock wave and the vapor front deflect the He−Ne laser beam, which is sensed by the photodiode and recorded on the oscilloscope. The oscilloscope, triggered by the laser pulse, measures the time lapse between the beginning of the laser pulse and the fluctuations of the probing beam.

The distance between the probing He−Ne laser beam and the specimen surface is adjusted by an x–y micrometer-stage from near zero to 500 μm. At different distances, the arrival times of the shock front and the vapor front are recorded. The measured distance–time relations are the transient locations of the shock front and the vapor front. The velocities of the shock wave and the vapor front are calculated by taking the time derivative of the transient locations. The optical components for focusing and detecting the He−Ne laser beam are set on a motion stage so that they are unaltered while the distance between the target surface and the probing beam is adjusted. Also, the excimer laser-focusing lens and the target are set on another one-motion stage so that adjusting the distance between the probing beam and the target surface would not change the intensity of the excimer laser beam at the target surface. The width of the nickel specimen is about 100 μm. This is to ensure that the width of the specimen is shorter than the depth of focus of the probing beam.

Figure 2 shows the experimental setup for measuring the transient transmissivity of a thin plasma layer with a thickness as small as a few micrometers. A probing beam is split from the excimer laser beam by a $CaF_2$ plate, and is directed to the center of the specimen by a dielectric mirror. The specimen is a 5 μm-thick, free-standing nickel foil. To measure the transmissivity of a thin plasma layer, a circular pinhole with a diameter, $d$ of 10 μm to 12 μm is fabricated at the center of the specimen. The transmission of the probing beam through the pinhole is measured. If the plasma layer is thicker than $\delta \tan(\theta) - d$, the entire probing laser beam passes through the plasma layer, and the path length of the probing beam in the plasma can be determined using straightforward geometry manipulations. Here $d$, $\delta$ and $\theta$ denote the thickness of the nickel film, the diameter of the pinhole, and the angle of the probing beam measured from the normal direction of the specimen, respectively. For a 5 μm-thick film with a pinhole diameter of 10 μm, and at the probing beam angle of 45°, transmission of the plasma layer with a minimum thickness of 5 μm ($\delta \tan(\theta) - d$) can be measured.

To reduce and eliminate signals from plasma emissions, the transmitted light is passed through a monochromator with a minimum wavelength bandwidth of 0.1 nm. The experiment verified that plasma emission is negligible when the minimum

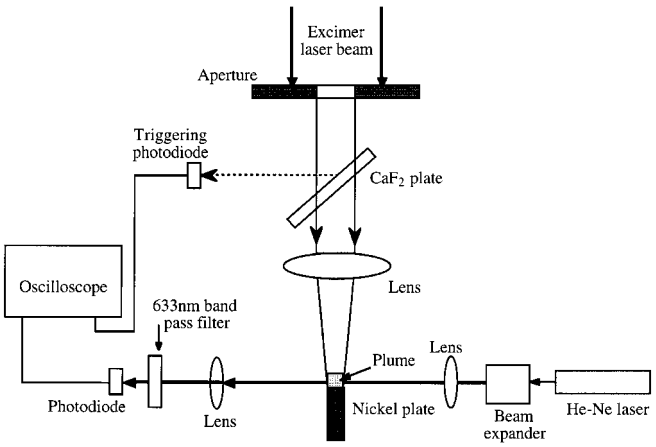


**Fig. 1.** Setup for the optical deflection measurement of the velocity of the laser-induced plasma front and shock front

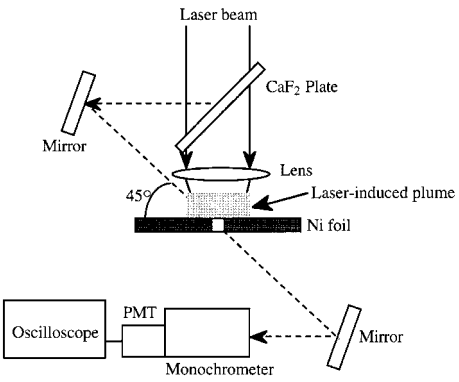


**Fig. 2.** Setup for the measurement of transient transmissivity of the laser-induced plasma

bandwidth of the monochromator is used – when the probing beam is blocked, the measured signal is at the noise level. A photomultiplier tube (PMT) is used to capture the transmitted light through the monochromator and record the transient intensity of the probing beam on an oscilloscope.

## 2 Calculation of the absorption coefficient of the laser-induced plasma

Analysis of the absorption coefficient of the laser-induced plasma requires thermodynamic properties of the laser-induced plasma. Based on the measured velocity of the laser-induced plasma, compressible gas dynamics is used to calculate the thermodynamic properties. The discontinuity above the target surface is treated using the Moth-Smith method [7, 8]. Figure 3 describes the one-dimensional flow of the laser-induced plume. The vertical axis represents the pressure distribution in different regions of the flow as a function of the distance from the target surface. Laser-evaporated particles are not in gas-dynamic equilibrium when they leave the target surface [9]. These particles form a Knudsen layer (KL), region I, where they establish thermodynamic equilibrium through collisions. The one-dimensional vapor flow after the Knudsen layer is described differently according to the Mach number of the flow at the exit of the Knudsen layer, that is, $M_{\mathrm{KL}} < 1$ or $M_{\mathrm{KL}} = 1$ [5, 7]. Calculations have shown that, for the laser intensities used in this work, the Mach number at the exit of the Knudsen layer equals unity. Therefore, the Knudsen layer, the rarefaction expansion region, the uniform vapor region, the compressed air region, and the ambient air region are formed successively from the surface, as shown in Fig. 3. Using the measured velocity of the laser-induced plume as the input to the gas dynamics model, the temperature, the pressure and the number density in each region can be calculated. Detailed procedures of the gas dynamics calculations are shown in the Appendix to Section 2 of this paper.

The thermodynamic properties obtained from the gas dynamics calculations are used to determine the absorption mechanisms in the laser-induced plume. Two different absorption mechanisms are considered, namely photo-ionization and photon–electron inverse-bremsstrahlung; other absorption processes have much smaller absorption coefficients for the laser intensity range used in this work [10].

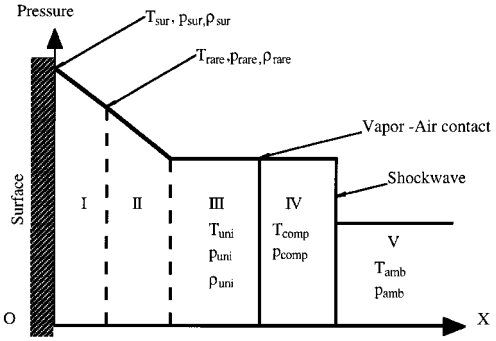


**Fig. 3.** Schematic regimes of vapor expansion: I: Knudsen layer, II: rarefaction expansion region, III: uniform vapor region, IV: compressed air, and V: ambient air

The absorption coefficient of the photo-ionization process is calculated as in [10]:

$$\kappa_{\mathrm{PI}} = \sum_{n}^{\infty} N_n \sigma_{\nu n} = \sum_{n}^{\infty} \left(7.9 \times 10^{-18}\right) \left(\frac{I_{\mathrm{H}}}{nh\nu}\right)^3 N_1 \times \exp\left[-\frac{I_{\mathrm{H}}}{k_B T}\left(1 - \frac{1}{n^2}\right)\right] \mathrm{cm}^{-1}, \quad (1)$$

where $N_n$ and $\sigma_{\nu n}$ are the number density and the cross-section at the energy level $n$, respectively. $N_1$ is the atom number-density at the ground state, $I_{\mathrm{H}}$ the ionization potential, $n$ the electronic energy level in the atomic structure, $\nu$ the frequency of the photon, $k_B$ the Boltzmann's constant, and $h$ Planck's constant. The summation is performed over the energy levels where the electron-binding energy is less than the photon energy of the excimer laser, since the ionization potential of nickel (7.635 eV) is higher than the photon energy of the excimer laser beam (5.0 eV). Multiple photon absorption or photo-ionization of ions is much less probable, therefore, is not considered in the calculation. With the temperature obtained from the gas dynamics analysis, the absorption coefficient of the photo-ionization process can be calculated from (1).

The inverse-bremsstrahlung absorption coefficient of an electron gas with a Maxwellian velocity distribution and a kinetic temperature $T_e$, is given [11] by:

$$\kappa_\nu = (3.69 \times 10^8) \frac{Z^3 N_+ N_{\mathrm{e}}}{T_e^{1/2} \nu^3} g_{ff} \mathrm{cm}^{-1}, \quad (2)$$

where $g_{ff}$ is the gaunt factor, which is assumed to be unity by Kramer's rule [11]. Usually, the number density of electrons, $N_{\mathrm{e}}$, and the number density of ions, $N_+$, are set to be equal, and the charge number, $Z$, is set to be 1.

The electrons participating in the inverse-bremsstrahlung absorption process are generated by both thermal ionization as well as photo-ionization. The number density of electrons due to thermal ionization is calculated by the Saha Equation [12]:

$$\frac{N_+ N_{\mathrm{e}}}{N} = 2 \left(\frac{2\pi m k_B T}{h^2}\right)^{3/2} \frac{U_+}{U} \exp\left(-\frac{I_H}{k_B T}\right), \quad (3)$$

where the electronic partition function of ions, $U_+$, is 1, $m$ is the atomic mass, and the electronic partition function of electrons, $U$, is given by [10]:

$$U = \sum_{n}^{\infty} 2n^2 \exp\left[-\frac{I_{\mathrm{H}} Z^2}{k_B T}\left(1 - \frac{1}{n^2}\right)\right] \quad (4)$$

The electrons generated by the photo-ionization process are not in thermal equilibrium, and the recombination process reduces the number densities of electrons and ions generated by photo-ionization. The rate of recombination is determined by the relaxation (recombination) time constant, $t_{\mathrm{r}}$. When the relaxation time constant is comparable to or longer than the duration of the laser pulse, the electrons generated by the photo-ionization process also contribute to photon–electron inverse-bremsstrahlung absorption. Therefore, this relaxation time constant needs to be evaluated, which is estimated [10]

as:

$$t_r = \frac{1}{2.7 \times 10^{-13} Z^2 T^{-3/4} N_e} . \quad (5)$$

The number densities of electrons and ions generated by photo-ionization at time $t$ can be calculated as:

$$N_e = \frac{1}{h\nu} \int_0^t \kappa(\xi) l(\xi) I(\xi) \exp(-\xi/t_r) \, d\xi , \quad (6)$$

where $\kappa$ and $l$ are the absorption coefficient and the thickness of the laser-induced plasma, respectively, $I$ is the laser intensity, and $h\nu$ the energy of each photon. The sum of the electron number densities calculated from (3) and (6) is used in (2) to calculate the absorption coefficient of the inverse-bremsstrahlung process. The total absorption coefficient of the laser-induced plume is the summation of the photo-ionization absorption coefficient and the inverse-bremsstrahlung absorption coefficient calculated from (1) and (2), respectively.

This calculated total absorption coefficient is used to compute the transmissivity of the laser beam in the laser-induced plasma. The transmissivity $\tau$ and the absorption coefficient $\kappa$ are related by Beer's law, since scattering of the laser beam by the plume has been determined to be negligible [13]. Thus:

$$\tau = \exp(-\kappa_{total} l / \cos(\theta)) , \quad (7)$$

in which, $l$ is the thickness of the plasma layer, and $\theta$ is the angle of incidence of the probing laser beam in the transmissivity measurement. The calculated and measured transmissivity are compared, and the comparison reveals the viability of the theoretical calculations and the absorption mechanism in the laser-induced plasma.

## 3 Results and discussions

### *3.1 Results of the plasma velocity measurement*

Figure 4 shows the signal recorded in the plasma-velocity measurement, as the laser-induced shock-front and the plasma deflect the probing beam. The data is obtained when the focal point of the probing beam is located 280 μm above the target surface, and the excimer laser intensity is 404 MW/cm$^2$. The excimer laser is fired at time zero. The intensity of the probing laser beam shows two fluctuations, at 32 ns and 36 ns. The charakteristics of the two fluctuations are different: the first fluctuation disappears within a few nanoseconds but the second fluctuation stays at a reduced level for a period longer than 200 ns (not completely shown in Fig. 4). Thus, the first fluctuation is caused by the shock wave, which is a thin layer of discontinuity in the optical refractive index [14], and the second fluctuation is caused by the laser-induced plasma plume. The time lapse between these two fluctuations is only 4 ns, indicating that the distance between the shock front and the vapor front is small. In fact, when the probing beam is located at distances closer to the target surface (less than 100 μm), these two fluctuations are indistinguishable since the distance between the shock front and the vapor front is less than the measurement resolution.

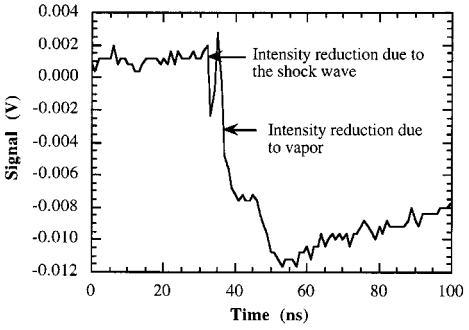


**Fig. 4.** Signal recorded in the optical deflection experiment The probing beam is at a distance of 280 μm from the surface and the laser intensity is 404 MW/cm$^2$

Figure 5 shows the transient locations of the plasma front at different laser intensities. At a given time, the plasma produced at a higher laser intensity travels farther away from the target surface than the plasma produced at a lower laser intensity. The velocity of the plasma front calculated from Fig. 5 is shown in Fig. 6. The measured vapor front velocities are of the same order of magnitude as other reported measurement or simulation results [15, 16]; however, our result also shows that, within different laser-intensity ranges, the plasma velocity varies differently with the laser intensity. For the two lowest laser intensities, 95 MW/cm$^2$ and 163 MW/cm$^2$, the location of the plasma front varies almost linearly with the laser intensity: after 13.4 ns the plasma fronts produced at intensities of 95 MW/cm$^2$ and 163 MW/cm$^2$ are, respectively, located at 20 μm and 35 μm. At the laser intensities between 199 MW/cm$^2$ and 348 MW/cm$^2$, the differences in the plasma front locations are small. At the highest laser in-

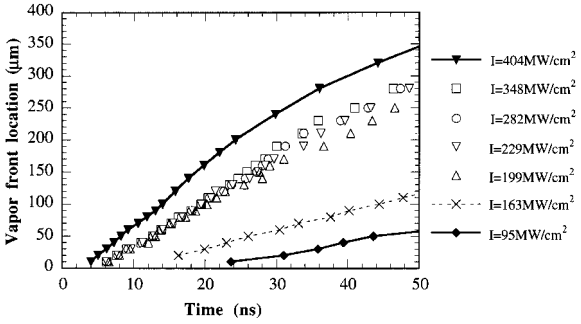


**Fig. 5.** Transient locations of the laser-induced plasma front

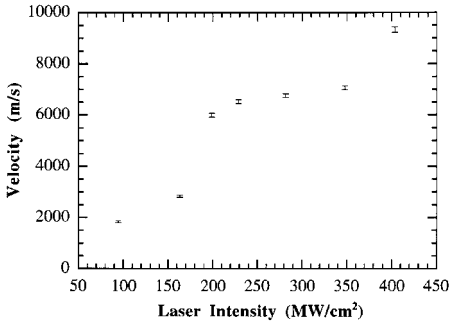


**Fig. 6.** Plasma front velocity at the end of the laser pulse (50 ns)

tensity, 404 MW/cm$^2$, the plasma front location is further away from those at lower laser intensities. For each laser intensity, the velocity of the plasma front decreases slightly within the duration of the laser pulse. The uncertainties of measuring the vapor front location and time are, respectively, 1 μm and 0.5 ns.

The time lapse between the beginning of the laser pulse and the onset of evaporation was also measured. When the probing beam is located at the target surface, the recorded time of the probing-beam fluctuation indicates when the plasma is generated. The onset of evaporation at different laser intensities also shows three distinctive regimes, as shown in Fig. 7. For the first two laser intensities, 95 MW/cm$^2$ and 163 MW/cm$^2$, the plume is generated at 17.8 ns and 12.1 ns respectively. For the next four laser intensities, varying between 199 MW/cm$^2$ and 348 MW/cm$^2$, the plume-generation times are almost identical, ranging between 4.5 ns and 4.2 ns. For the highest laser intensity, 404 MW/cm$^2$, the plume is generated at 2.2 ns. The uncertainty of this measurement is determined by the time resolution of the oscilloscope, 0.5 ns.

The result of this velocity measurement suggests that there are different *laser–target* coupling mechanisms within the laser-intensity range used in this work. Although the plume expansion results from both the laser–target and the laser–plume interactions, generation of plume depends solely on the laser–target interaction. At low intensities, the onset of evaporation decreases linearly with laser intensity, indicating that thermal evaporation (heterogeneous bubble nucleation) occurs at the target surface. This is because the time required to reach the evaporation temperature decreases almost linearly with the laser intensity when the liquid/vapor phase transformation occurs at the material's surface. For medium laser intensities (199–348 MW/cm$^2$), the phase-change mechanism could be in transition from the heterogeneous bubble nucleation to the explosive superheating phase transformation [17, 18]. The explosive phase-change occurs when the temperature of the material is raised rapidly close to the critical point and thus the material is abruptly evaporated. In this case, the absorbed laser energy is conducted to the molten pool, heating the melt to the temperature near the critical point and inducing explosive evaporation. When the laser intensity varies from 348 MW/cm$^2$ to 404 MW/cm$^2$, the plume generation time is reduced by half. This suggests the explosive phase change dominates the evaporation mechanism when the laser intensity is higher than 350 MW/cm$^2$ – it takes a shorter period of time for the molten material to reach the critical temperature when the laser intensity is above a certain value. However, more experimental evidence, such as surface temperature measurement, is needed to verify the above assumptions concerning the mechanisms of high-power laser evaporation processes.

### *3.2 Results of the transmissivity measurement*

Figure 8 shows a pair of reference and transmission signals when the laser intensity is at 163 MW/cm$^2$. The reference signal is obtained by recording the probing signal going through the pinhole in the specimen (Fig. 2) while the ablation laser beam is blocked from the target surface. The transmission signal is the intensity of the probing beam when the probing beam passes through the laser-induced plasma layer. The negative voltage results from the PMT circuit. The total time duration of the measurement is the laser-pulse duration, which is approximately 50 ns with FWHM of 26 ns. Both the transmission and the reference signals appear rather smooth. This is because of the relatively short time-resolution of the PMT used in this work, which is 3 ns. The ratio between the transient transmission and the reference signals is the transient transmissivity of the plasma at the incident laser intensities.

Figure 9 shows the transient transmissivity of the plasma layer at different laser intensities. The transmissivity remains at unity for the first several nanoseconds, which corresponds to the time period before the generation of the plume. The plasma-generation time obtained in this experiment matches that measured by the optical deflection technique (Fig. 7). For a certain laser intensity, the transmissivity of the plume decreases with time. The variation of transmissivity with laser intensity also shows three regions: the transmissivities are almost identical for the laser intensities between 199 MW/cm$^2$

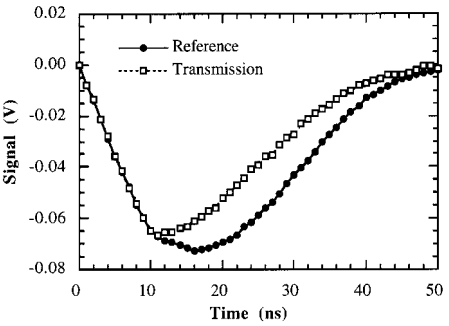


**Fig. 8.** Reference and transmission signals in the transmissivity measurement

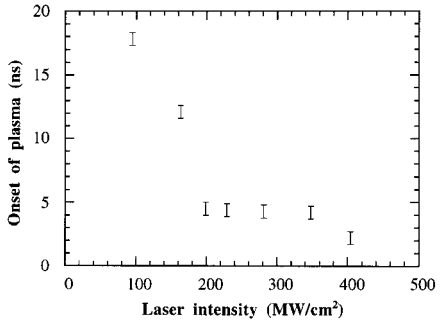


**Fig. 7.** Onset of the laser-induced plasma

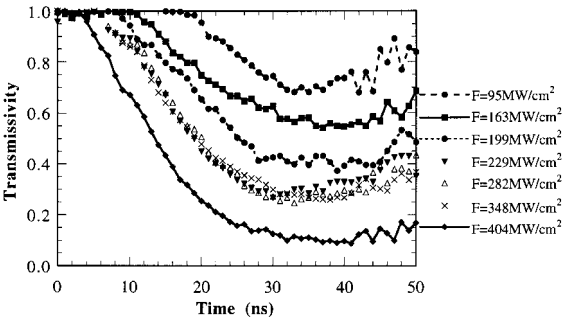


**Fig. 9.** Transient transmissivity of the laser-induced plasma

and 348 MW/cm$^2$, and this laser intensity range corresponds to the same ranges in which the plasma velocity and the onset of evaporation change little with laser intensity. As shown in Fig. 9, the uncertainty in measuring the transmissivity is small before 40 ns, while fluctuations can be seen between 45 ns and 50 ns due to the weak probing signals near the end of the laser pulse.

The plasma velocity and transmissivity depend strongly on the conditions at the target surface. The optical characteristics of the surface, including diffuse reflectivity and specular reflectivity, were measured [13]. The energy of the laser beam absorbed and scattered by the plasma, and the energy absorbed and scattered at the target surface, have also been measured. These measurement results were used in a radiative transfer analysis to reveal the amount of laser energy absorbed by the target, absorbed by the plasma, and lost to the ambient atmosphere through plasma scattering and surface reflection. Detailed results have been presented elsewhere [13].

### *3.3 Results of the gas dynamics analysis*

The measured plasma front velocity is used as the input parameter in the gas dynamics analysis to calculate the thermodynamic properties of the laser-induced plume. Figure 10 shows the calculated temperature, pressure and number density at the target surface and in the plasma plume, with laser intensities between 95 MW/cm$^2$ and 404 MW/cm$^2$. The velocity at the end of the laser pulse is used in this calculation; the thermodynamic parameters shown in Fig. 10 therefore represent the values at the end of the laser pulse. The subscripts 's' and 'v' in the key to the graphs denote the parameters at the target surface and in the vapor, respectively.

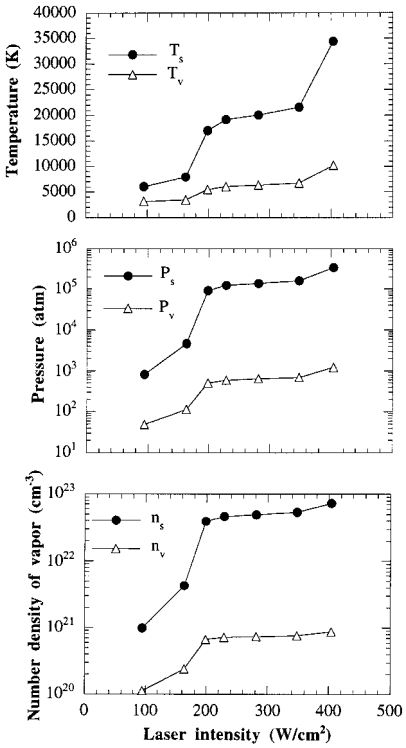


**Fig. 10.** Results of gas dynamics calculations

The temperature, pressure and number density increase rapidly when the laser beam intensity is increased from 95 MW/cm$^2$ to 199 MW/cm$^2$, and from 348 MW/cm$^2$ to 404 MW/cm$^2$. However, variations of these parameters are small when the laser beam intensity varies between 199 MW/cm$^2$ and 348 MW/cm$^2$.

It should be noticed that the surface temperature is near the critical temperature for nickel (7180 K [17]) at the two lowest laser intensities, and is higher than the critical temperature at higher laser intensities. Such high temperatures were also obtained by others, who used a similar method [5, 19]. The calculated surface temperatures agree qualitatively with the assumptions on the mechanisms of laser-induced evaporation. Based on the measurements of the onset of evaporation, it is assumed that the target surface undergoes heterogeneous boiling at low laser intensities, and reaches critical temperature and induces homogeneous boiling (explosive evaporation) at high laser intensities. Again, further investigation is needed to verify the assumptions on the laser-evaporation mechanisms.

The absorption coefficients of the photo-ionization and the inverse-bremsstrahlung processes are calculated using the procedures described in Sect. 2. Figure 11 shows the electron number density, the ionization ratio, and the absorption coefficients of the photo-ionization and the inverse-bremsstrahlung processes. The electron number density shown in the figure is the total electrons generated by both the thermal ionization process and the photo-ionization process at the end of the laser pulse (50 ns). The calculation shows that the electron-to-neutral ratio (the ionization ratio) at the end of the laser pulse is rather small, varying from less than 0.1% at 95 MW/cm$^2$ to a few percentage points at 404 MW/cm$^2$.

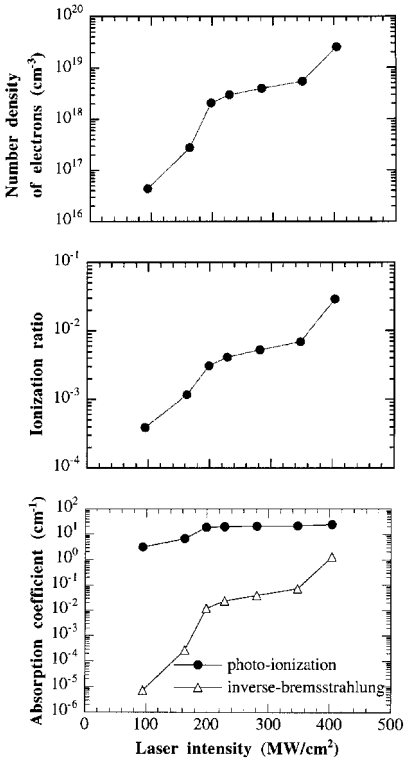


**Fig. 11.** Calculated electron number density, ionization ratio and absorption coefficient at different laser intensities

In Fig. 11, the absorption coefficients by inverse bremsstrahlung and photo-ionization are calculated using (2) and (1). The inverse-bremsstrahlung absorption coefficient, $\kappa_{\mathrm{IB}}$, increases by six orders of magnitude within the laser intensity range used in this work. This is because the inverse-bremsstrahlung process depends on the number density of electrons in the plasma, which varies exponentially with the temperature of the plasma. On the other hand, the photo-ionization absorption coefficient, $\kappa_{\mathrm{PI}}$, increases less than one order of magnitude since it is directly proportional to the number density of neutrals, which does not vary drastically with laser intensity. It can thus be seen that, compared with the absorption coefficient of photo-ionization, the absorption coefficient due to inverse bremsstrahlung is several orders of magnitude smaller. Clearly, the photo-ionization absorption process is the dominant absorption mechanism within this laser intensity range.

### *3.4 Comparison between the results of gas dynamics calculations and the results of experimental measurements*

A direct comparison between the measured and the calculated values is needed to verify the calculation results. In this work, the measured transmissivity of the laser-induced plasma is compared with the value calculated from the total absorption coefficient. The comparison between the measured and the calculated transmissivity at the end of the laser pulse is shown in Fig. 12. Although a number of assumptions and simplifications have been made in calculating the thermodynamic properties and the theoretical absorption coefficients, it can be seen that the calculated transmissivity generally matches the measured value. In the middle range of the laser intensities, the calculated and measured transmissivities show good agreement, while for the low laser intensities, the differences are noticeable. For the whole laser intensity range, the calculation predicts higher transmissivity values than the measurement, indicating that the calculation has not accounted for other extinction mechanisms of the laser beam in the plume as well as any inaccuracy in the model for computing the thermodynamic properties of the plume.

Another possible reason for the calculated transmissivity being higher than the measured value is that the thickness of the plasma layer might be increased by plasma filling the diagnostic pinhole or even penetrating to the rear side of the specimen. The number density of the vapor at the back side of the specimen is expected to be small since the vapor diffuses into a larger space. Therefore, the effect of plasma penetrating through the pinhole can be neglected. On the other hand, it is possible that the pinhole is filled with plasma at the end of the laser pulse, when the calculated and measured data are compared. At the end of the laser pulse, the measured thickness of the plasma at the front side of the specimen varies from about 50 μm at the lowest laser intensity, to about 400 μm at the highest laser intensity (Fig. 5). Since the thickness of the specimen is only 5 μm, neglecting filling of the plasma in the pinhole would cause a maximum error of 10% when calculating the thickness of the plasma, corresponding to a 1% error in the transmissivity calculation. Thus, the effect of plasma filling the pinhole is judged to be negligible.

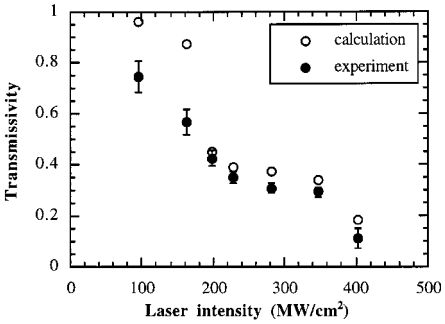


**Fig. 12.** Comparison between the calculated and the measured transmissivity at $t = 50$ ns

## 4 Conclusions

Interaction between the laser-induced plasma plume and the laser beam was investigated by optical measurements of the plasma velocity and transmissivity. The thermodynamic properties, including the plume temperature, pressure, and the number density of total particles, were estimated using a one-dimensional gas dynamics analysis, with the measured plasma velocity as the input parameter. The mechanisms of laser–plasma interaction were assessed by calculating the absorption coefficients of photo-ionization and inverse-bremsstrahlung processes. It was found that, within the laser fluence range used in this work, photo-ionization was the dominant absorption process. Computations of the thermodynamic parameters and the absorption coefficients were verified by comparing calculated and measured transmissivities.

It was also found that the vapor-front velocity, the onset of vaporization and the plasma transmissivity did not vary linearly with the laser beam intensity. Within the range of laser intensity, 200–350 MW/cm$^2$, these three parameters did not change significantly. This result suggests that there are different mechanisms governing the removal process of the target material. Further investigations are necessary to understand fully the different ablation phenomena.

## Appendix to Section 2: Gas dynamics analysis of the laser-induced plume

The velocity distribution of thermally evaporated particles is described by the Maxwellian distribution function [9]:

$$f_{\mathrm{sur}}^{+} = n_{\mathrm{sur}} \left( \frac{m_{\mathrm{Ni}}}{2\pi k_B T_{\mathrm{sur}}} \right)^{3/2} \frac{E_{\mathrm{I}}^{j/2-1}}{\Gamma(j/2)(k_B T_{\mathrm{sur}})^{j/2}} \times \exp\left\{ -\frac{1}{k_B T_{\mathrm{sur}}} \left[ \frac{m_{\mathrm{Ni}}}{2} (\mathrm{v}_x^2 + \mathrm{v}_y^2 + \mathrm{v}_z^2) + E_{\mathrm{I}} \right] \right\} \quad \text{for} \quad \mathrm{v}_x \geq 0,\ -\infty < \mathrm{v}_y,\ \mathrm{v}_z < +\infty\,. \tag{A.1}$$

Here $E_{\mathrm{I}}$ is the total energy of the gas, $j$ is the number of internal degree of freedom, and $\Gamma$ is the gamma function. The

velocity distribution at the exit of the Knudsen layer is described by a displaced Maxwellian distribution function [9]:

$$f_{\mathrm{KL}}^{\pm} = n_{\mathrm{KL}} \left(\frac{m_{\mathrm{Ni}}}{2\pi k_B T_{\mathrm{KL}}}\right)^{3/2} \frac{E_{\mathrm{I}}^{j/2-1}}{\Gamma(j/2)(k_B T_{\mathrm{KL}})^{j/2}} \times \exp\left\{-\frac{1}{k_B T_{\mathrm{KL}}}\left[\frac{m_{\mathrm{Ni}}}{2}\left[(\mathrm{v}_x - u_{\mathrm{KL}})^2 + \mathrm{v}_y^2 + \mathrm{v}_z^2\right] + E_{\mathrm{I}}\right]\right\}$$
$$\text{for} \quad -\infty < \mathrm{v}_x,\ \mathrm{v}_y,\ \mathrm{v}_z < +\infty\,, \tag{A.2}$$

where $u_{\mathrm{KL}}$ is the velocity of the plume at the exit of the Knudsen layer and $f_{\mathrm{KL}}^{\pm}$ is the velocity distribution function with both positive and negative directions. For back-scattering of the evaporated particles, the velocity distribution function of particles at the target surface is

$$f_{\mathrm{sur}} = \begin{cases} f_{\mathrm{sur}}^{+} & \mathrm{v}_x > 0 \\ \beta f_{\mathrm{KL}}^{\pm} & \mathrm{v}_x < 0 \end{cases}\,, \tag{A.3}$$

where $\beta$ is solved by the mass-conservation requirement. The conservation equations of mass, momentum and energy are used to establish the relationship between the thermodynamic properties at the target surface and at the exit of the Knudsen layer [7, 8]:

$$\frac{T_{\mathrm{KL}}}{T_{\mathrm{sur}}} = \left\{\left[1 + \pi\left(\frac{\gamma_{\mathrm{Ni}}-1}{\gamma_{\mathrm{Ni}}+1}\frac{\alpha}{2}\right)^2\right]^{\frac{1}{2}} - \sqrt{\pi}\frac{\gamma_{\mathrm{Ni}}-1}{\gamma_{\mathrm{Ni}}+1}\frac{\alpha}{2}\right\}^2, \tag{A.4a}$$

$$\frac{\varrho_{\mathrm{KL}}}{\varrho_{\mathrm{sur}}} = \frac{N_{\mathrm{KL}}}{N_{\mathrm{sur}}} = \left(\frac{T_{\mathrm{KL}}}{T_{\mathrm{sur}}}\right)^{\frac{1}{2}}\left[\left(\alpha^2\frac{1}{2}\right)\mathrm{e}^{\alpha^2}\,\mathrm{erfc}(\alpha) - \frac{\alpha}{\sqrt{\pi}}\right] + \frac{1}{2}\frac{T_{\mathrm{KL}}}{T_{\mathrm{sur}}}\left[1 - \sqrt{\pi}\alpha\mathrm{e}^{\alpha^2}\,\mathrm{erfc}(\alpha)\right], \tag{A.4b}$$

$$\alpha = M_{\mathrm{KL}}(\gamma_{\mathrm{Ni}}/2)^{1/2}, \quad \text{and} \tag{A.4c}$$

$$\beta = \left[(2\alpha^2+1) - \alpha\left(\frac{\pi T_{\mathrm{KL}}}{T_{\mathrm{sur}}}\right)^{1/2}\right]\mathrm{e}^{\alpha^2}\frac{\varrho_{\mathrm{KL}}}{\varrho_{\mathrm{sur}}}\left(\frac{T_{\mathrm{KL}}}{T_{\mathrm{sur}}}\right)^{\frac{1}{2}}, \tag{A.4d}$$

where the local sound velocity, $a_{\mathrm{KL}} = \sqrt{\gamma_{\mathrm{Ni}} k_B T_{\mathrm{KL}}/m_{\mathrm{Ni}}}M_{\mathrm{KL}}$ denotes the mach number which is the ratio of the local velocity, $u_{\mathrm{KL}}$, to the local sonic velocity, $a_{\mathrm{KL}}$. The ratio of specific heat, $\gamma_{\mathrm{Ni}}$, is 5/3 since the plume is assumed to be a monatomic ideal gas. $T_{\mathrm{KL}}$ and $\varrho_{\mathrm{KL}}$ are equal to $T_{\mathrm{rare}}$ and $\varrho_{\mathrm{rare}}$ [7].

The sound velocity and pressure ratio across the isentropic expansion region is [8]:

$$\frac{a_{\mathrm{rare}}}{a_{\mathrm{uni}}} = \left(\frac{p_{\mathrm{rare}}}{p_{\mathrm{uni}}}\right)^{(\gamma_{\mathrm{Ni}}-1)/2\gamma_{\mathrm{Ni}}} = \frac{2}{\gamma_{\mathrm{Ni}}+1} + \frac{\gamma_{\mathrm{Ni}}-1}{\gamma_{\mathrm{Ni}}+1}M_{\mathrm{uni}} \tag{A.5}$$

The ratio of the sound velocity is directly related to the ratio of the temperature since $a = \sqrt{\gamma_{\mathrm{Ni}} k_B T/m_{\mathrm{Ni}}}$.

The compressed air region induces a shock wave that propagates into the quiescent ambient air. The velocity of the compressed air behind the shock wave is formulated by the Rankine–Hugoniot equation [20]:

$$\mathrm{v}_{\mathrm{comp}} = a_{\mathrm{amb}}\left(\frac{p_{\mathrm{comp}}}{p_{\mathrm{amb}}} - 1\right) \Big/ \gamma_{\mathrm{air}}\sqrt{1 + \frac{\gamma_{\mathrm{air}}+1}{2\gamma_{\mathrm{air}}}\left(\frac{p_{\mathrm{comp}}}{p_{\mathrm{amb}}} - 1\right)} \tag{A.6a}$$

where $\gamma_{\mathrm{air}} = 1.4$ is the ratio of specific heats of air. The pressure and the velocity in the uniform nickel vapor region and in the compressed air region are assumed to be equal:

$$\mathrm{v}_{\mathrm{uni}} = \mathrm{v}_{\mathrm{comp}} \text{ and } p_{\mathrm{uni}} = p_{\mathrm{comp}} \tag{A.6b}$$

The gas dynamic parameters at the uniform vapor region, such as $M_{\mathrm{uni}}$ and $p_{\mathrm{uni}}$, are directly related to the ambient air pressure, $p_{\mathrm{amb}}$, and the ambient sonic velocity, $a_{\mathrm{amb}}$, by ((A.6a) and (A.6b)):

$$\frac{p_{\mathrm{uni}}}{p_{\mathrm{amb}}} = 1 + \gamma_{\mathrm{air}}M_{\mathrm{uni}}\frac{a_{\mathrm{uni}}}{a_{\mathrm{amb}}}\left[\frac{\gamma_{\mathrm{air}}+1}{4}M_{\mathrm{uni}}\frac{a_{\mathrm{uni}}}{a_{\mathrm{amb}}} + \sqrt{1 + \left(\frac{\gamma_{\mathrm{air}}+1}{4}M_{\mathrm{uni}}\frac{a_{\mathrm{uni}}}{a_{\mathrm{amb}}}\right)^2}\right] \tag{A.6c}$$

Using (A.1) to (A.6), the gas dynamic parameters in each region can be evaluated with the measured velocity of the vapor front as the known parameter. The procedures of the calculation are as follows:

1. Assuming a value for $T_{\mathrm{uni}}$, and using the measured velocity of $\mathrm{v}_{\mathrm{uni}}$, the Mach number in the uniform vapor region is calculated from the definition: $M_{\mathrm{uni}} = \mathrm{v}_{\mathrm{uni}}/a_{\mathrm{uni}} = \mathrm{v}_{\mathrm{uni}}/\sqrt{\gamma_{\mathrm{Ni}} k_B T_{\mathrm{uni}}/m_{\mathrm{Ni}}}$. The pressure in the uniform vapor region is then calculated from (A.6c).
2. Using the thermodynamic properties obtained from step 1, the thermodynamic ptoperties in the rarefaction region can be calculated from (A.5).
3. Using the thermodynamic properties in the rarefaction region from step 2, the thermodynamic properties at the target surface can be calculated from (A.4).
4. Iteration is carried out until the temperature and the pressure at the surface, calculated from step 3, satisfy the Clausius–Claypeyron equation:

$$p_{\mathrm{sur}} = \exp\left[\frac{m_{\mathrm{Ni}}\Delta H}{RT_b}\left(1 - \frac{T_b}{T_{\mathrm{sur}}}\right)\right] \tag{A.7}$$

where $R$ is the universal gas constant, and $\Delta H$ is heat of fusion.

*Acknowledgements.* Partial support of this work by the National Science Foundation under the Grant no. CTS- 9624890 is greatly acknowledged.

## References

1. T.E. Mills, P.J. Bishop, A. Mirnardi: AIAA J. Thermophysics Heat Transfer **8**, 223 (1994)
2. V.K. Goncharov, V.I. Karaban: Zhurnal Priklandnoi Spekroskopii **45**, 22 (1986)
3. R.S. Patel, M.Q. Brewster: J. Heat Transfer **112**, 170 (1990)
4. R.K. Singh, J. Narayan: Phys. Rev. B **41**, (1990)
5. C.L. Chan, J. Mazumder: 1989 J. Appl. Phys. **62**, 4579 (1987)
6. A. Vertes, R.W. Dreyfus, D.E. Platt: IBM J. Res. Develop. **38**, 3 (1994)
7. C.J. Knight: AIAA J. Thermophysics Heat Transfer **17**, 519 (1979)

8. M. Aden, E. Beyer, G. Herziger: J. Phys. D **23**, 655 (1990)
9. R. Kelly, R.W. Dreyfus: Nucl. Instrum. Method Phys. Res. B **32**, 341 (1988)
10. Y. Zel'dovich, Y. Raiser: *Physics of Shock Waves and High-Temperature Hydrodynamic Phenomena* (Academic Press, New York and London, 1966)
11. L. Spitzer: *Physics of Fully Ionized Gases*, 2nd Ed. (John Wiley & Sons, New York, 1962)
12. F. Chen: *Introduction to Plasma Physics and Controlled Fusion*, (Plemon, New York, 1984)
13. X. Xu, K.H. Song: J. Heat Transfer, in press (1997)
14. A.M. Azzeer, A.S. Al-Dwayyan, M.S. A1-Salhi, A.M. Kamal, M.A. Harith: Appl. Phys. B **63**, 307 (1996)
15. D.B. Geohegan: Appl. Phys. Lett. 60, **22**, 2732 (1992)
16. J.N. Leboeuf, K.R. Chen, J.M. Donato, D.B. Geohegan, C.L. Liu, A.A. Puretzky, R.F. Wood: Appl. Surf. Sci. **96**, 14 (1996)
17. M. Martynyuk: Russian J. Phys. Chem. **57**, 4, 494 (1983)
18. A. Miotello, R. Kelly: Appl. Phys. Lett. **67**, 24, 3535 (1995)
19. J.J. Chang, B.E. Warner: Appl. Phys. Lett. **69**, 4, 473 (1996)
20. H.W. Leipmann, A. Roshko: *Elements of Gas Dynamics*, Ch. 1, (John Wiley & Sons, New York, 1957)